



High-performance water electrolyzer with minimum platinum group metal usage: Iron nitride–iridium oxide core–shell nanostructures for stable and efficient oxygen evolution reaction

Hui-Yun Jeong ^{a,1,2}, Jinho Oh ^{a,b,1}, Gyu Seong Yi ^{a,c}, Hee-Young Park ^a, Sung Ki Cho ^a, Jong Hyun Jang ^a, Sung Jong Yoo ^{a,b,d,*}, Hyun S. Park ^{a,b,d}

^a Center for Hydrogen-Fuel Cell Research, Korea Institute of Science and Technology (KIST), Seoul 02792, Republic of Korea

^b Division of Energy & Environment Technology, KIST School, University of Science and Technology (UST), Daejeon 34113, Republic of Korea

^c School of Chemical and Biological Engineering, Seoul National University (SNU), Seoul 08826, Republic of Korea

^d KHU-KIST Department of Converging Science and Technology, Kyung Hee University, Seoul 02447, Republic of Korea



ARTICLE INFO

Keywords:

Proton exchange membrane water electrolysis
Electrocatalysts
Oxygen evolution reaction
Core-shell structures

ABSTRACT

To reduce the usage of rare-earth metals in a proton-exchange-membrane water electrolyzer (PEMWE), a highly active water-oxidizing anode based on a core–shell catalyst structure was developed. Earth-abundant metal-based iron-nitride nanostructure was adopted to support thin, electrodeposited iridium-oxide films. PEMWEs with core–shell nanostructure has substantially low ohmic and mass-transfer resistances, suggesting that the introduction of Fe₂N nanostructure on Ti PTL enhances the transfer of protons, water, and oxygen on the catalyst layer. Furthermore, a high Ir mass activity of 103 A/mg_{Ir} was achieved with reduced Ir loading of 0.036 mg/cm² on the Ti PTL. The well-known weakness of transition-metal nitrides (TMNs) for use in PEMWEs, that is, their chemical instability in corrosive acidic environments, was overcome by carefully passivating the surfaces of the TMNs with chemically stable Ir catalyst layers. As a result, the prepared core–shell-structured catalysts were stable under the PEMWE operating condition.

1. Introduction

The conversion of electrical energy into chemical energy in the form of fuels is an economically and environmentally sustainable solution for storing and transporting the energy obtained from renewable energy systems. Electrochemical energy conversion techniques are beneficial for the storage of the surplus peak energy from fluctuating renewable energy sources which are also known as power-to-X technologies. Producing hydrogen by electrochemical water electrolysis has been suggested as one of a promising method to distribute electricity combined with hydrogen fuel cells [1,2]. Among several types of water electrolyzers, proton-electrolyte-membrane water electrolyzers (PEMWE) have many advantages compared to well-established alkaline water electrolyzers, including compact cell design, high current density, high purity of the produced hydrogen, and rapid operational response to fluctuating renewable power sources [3,4].

However, the development of enhanced electrocatalysts and optimization of their electrode structure is still of great importance for the practical and widespread deployment of PEMWEs [5]. Usually, carbon-supported platinum catalysts (Pt/C) are used as cathode materials for the hydrogen evolution reaction (HER), while iridium (Ir)-based catalysts are used as anode materials for the oxygen evolution reaction (OER). In particular, the scarcity and high price of Ir are considered to be bottlenecks inhibiting the large-scale commercialization of PEMWE [6]. Compared with Pt, a rare-earth metal with a low production rate of 150–200 tons per year, Ir availability is extremely limited, as only a few tons per year are produced [7]. Making matters worse, while the necessary Pt loadings on the cathode are comparatively small (<0.3 mg/cm²) owing to the fast HER kinetics and high of the catalysts on conductive carbon supports (i.e., Pt/C), a higher amount of Ir (\geq a few mg/cm²) is required on the anode owing to the sluggish OER kinetics and inefficient material utilization without appropriate catalyst and

* Corresponding authors at: Center for Hydrogen-Fuel Cell Research, Korea Institute of Science and Technology (KIST), Seoul 02792, Republic of Korea.
E-mail addresses: ysj@kist.re.kr (S.J. Yoo), hspark@kist.re.kr (H.S. Park).

¹ These authors contributed equally.

² Present address: Materials Science Division, Lawrence Livermore National Laboratory, Livermore, CA, 94550 USA

electrode engineering [4,8]. However, it is envisioned that the Ir loading on the anode should be lowered (e.g., to 0.05 mg/cm²) to meet the annual demand on the PEMWE system installation on the scale of ≈ 5 GW by 2040 [6]. Thus, the development of an anode with an optimized Ir catalyst structure using a minimum iridium loading is of great importance to enable industrial-scale application of PEMWES.

Among the various methods for preparing Ir catalysts, electrodeposition allows a direct, facile deposition of iridium catalysts on conductive porous transport layers (PTLs) in a controlled manner. Lee et al. electrodeposited a thin iridium oxide (IrO_x) layer on a carbon-based PTL (carbon paper) and investigated its OER performance in a PEMWE. A high water-splitting current density of 1.92 A/cm² was achieved at 1.8 V using a Nafion 212 membrane (operated at 90 °C) with low iridium loading of 0.1 mg_{Ir}/cm² [9]. However, as carbon paper was used as the anode PTL, carbon corrosion via carbon oxidation led to the low stability of the PEMWE. To avoid this problem, Choe et al. adopted a porous titanium substrate instead of carbon paper and electrodeposited an IrO_x layer on a Ti porous transport layer (Ti PTL) [10]. It was suggested that the IrO_x layer acts not only as a catalyst but also as a corrosion-resistant layer for the Ti PTL. The PEMWE fabricated with the IrO_x-coated Ti PTL and Nafion 212 membrane exhibited a current density of 0.97 A/cm² at 1.6 V and 120 °C using an iridium loading of 0.4 mg_{Ir}/cm².

Although PEMWEs with relatively high current densities have been obtained using electrodeposited iridium oxide films (EIROFs), their PEMWE performance still requires enhancement using a reduced Ir loading. Considering the current status of PEMWE performance (0.3–0.6 g_{Ir}/kW based on an Ir loading of 1–2 mg_{Ir}/cm²), installation of an industrial 5 GW scale electrolyzer requires a 1.6–3.3 tons of Ir which is close to global production of iridium [6]. In order to significantly reduce the cost of PEMWEs, a high mass activity of Ir should be realized, thereby minimizing the amount of Ir required in the PEMWE. In this respect, the apparent activity of the EIROFs is low, as planar iridium-oxide layers are formed with a limited electrochemically active surface area (ECSA), resulting in low Ir mass activity. The development of core–shell-structured catalysts is a straightforward solution to achieve high specific activities of the elements of interest [11]. This is because only the surface atoms of catalysts are involved in the reaction, and the substitution of inner Ir atoms with inexpensive metal atoms reduces Ir usage while maintaining the surface-exposed Ir active sites. Lim et al. fabricated Pt@EIROF core-shell structured on a Ti PTL by sequentially electrodepositing Pt and IrO₂ [12]. With increased surface roughness of Ti PTL caused by Pt particles, a higher water-oxidation current than that of the EIROF-coated Ti PTL can be achieved. However, as Pt is also a rare-earth metal with a low natural abundance, the use of earth-abundant-metal-based electrodes is necessary to reduce the production cost of PEMWEs.

Early transition-metal nitrides (TMNs) are ideal core materials for electrochemical applications, as they show superior electrical conductivity compared with their oxide counterparts [13]. As Fe, Co, and Ni nitrides exhibit poor chemical stability under acidic electrochemical conditions, their application as OER catalysts is usually limited to basic electrochemical conditions [14]. However, when the surfaces of TMNs are passivated by chemically stable platinum-group metal layers, the produced core–shell-structured catalysts demonstrate high stability under acidic and oxidative conditions and also achieve high mass activity of platinum group metals [15–18]. In this research, iron nitride (Fe₂N) was chosen as the earth-abundant core material to support thin EIROF. Fe₂N nanostructure was deposited on the Ti PTL by hydrothermal iron-oxide deposition followed by nitridation. Owing to the increased surface area of the Fe₂N nanostructure decorated on the Ti PTL, a thinner EIROF with a high surface area can be produced using the same amount of Ir as the EIROF on the conventional Ti PTL. The performance and stability of membrane electrode assemblies (MEAs) comprised of a conventional EIROF-coated Ti PTL and Fe₂N-coated Ti PTL were compared.

2. Experimental

2.1. Preparation of water oxidation anode for electrolyzer

Iron-oxide nanorods were deposited on a porous titanium transport layer (Ti PTL; Bekaert 2GDL9N-025, porosity 60%, 250 μm) using a hydrothermal method. A 60 mL aqueous solution of 3 mmol FeCl₃ 6 H₂O and 3 mmol Na₂SO₄ was transferred to a 100 mL Teflon-lined stainless-steel hydrothermal reactor. The Ti PTL was cut to a size of 2 × 3 cm², and one the side that would be placed in electric contact with the bipolar plate was passivated with polyimide tape to prevent the growth of iron oxide. The substrates were placed in a Teflon liner at a certain angle with the surface of interest facing downward. The Teflon liner was sealed in a stainless steel autoclave. The autoclave was then placed in a furnace and heated at 120 °C for 8 h. After the hydrothermal reaction, the substrate was thoroughly washed with DI water and dried in a drying oven at 70 °C.

To nitridate the iron-oxide nanorods, the substrates were transferred to a tube furnace, which was vacuum-purged and filled with NH₃ gas. The furnace was then heated to 450 °C at a ramp rate of 2.5 °C/min, and the temperature was maintained at 450 °C for 3 h with a flow of 200 sccm NH₃. After completion of the nitridation reaction, the tube furnace was cooled to room temperature, and the substrates were collected after purging NH₃ with Ar gas. A solution for iridium deposition was prepared by following Yamanaka's method with slight modification [19–21]. First, 0.133 g of iridium(IV) chloride hydrate and 0.2 g of oxalic acid dihydrate, which acts as a stabilizing ligand to prevent the precipitation of IrO₂, was dissolved in 35 mL of deionized (DI) water. Then, 0.4 mL of aqueous H₂O₂ (30%) was added dropwise to the iridium solution, followed by the dropwise addition of 2.21 g (16 mmol) of potassium carbonate dissolved in DI water (5 mL). The as-prepared solution was stirred in a 30 °C water bath for 4 days until the solution became deep blue.

An electrodeposited iridium-oxide film (EIROF) was deposited on the PTL using a chronoamperometric method. Constant potential experiments were conducted using a saturated calomel electrode (SCE) as the reference electrode and carbon paper as the counter electrode. The bare Ti PTL or Fe₂N-coated Ti PTL were immersed in a bath containing a deep-blue iridium electroplating solution, and a constant potential of 0.7 V vs. SCE was applied for the desired electrodeposition time (1, 3, 5, and 10 min). Prior to electrodeposition at the bare Ti PTL, the titanium surface was pretreated in a 5% (w/v) oxalic acid solution at 75 °C for 15 min

2.2. Characterization of prepared electrodes

The crystal structures of the catalysts were analyzed using X-ray diffraction (D8 Advance, Bruker). The surfaces of the catalysts were characterized using X-ray photoelectron spectroscopy (XPS, K-alpha, Thermo Scientific) based on a Kα (1486.6 eV) radiation source. The XPS spectra were calibrated by correcting the C–C peak position of the C1s peak of adventitious carbon to 284.8 eV. The Ir content of the prepared PTL was determined using inductively coupled plasma atomic-emission spectroscopy (ICP-AES, Optima 7300DV, PerkinElmer). As ICP-AES measurements require the digestion of a solid sample into a solution, iridium was dissolved using the microwave digestion method using aqua regia.

The morphologies of the electrocatalysts on the Ti PTL were analyzed using a scanning electron microscope (SEM; Teneo VS, Field Emission Inc.). Energy-dispersive spectrometry (EDS) line-scanning analyses were conducted using a high-resolution SEM (Regulus 8230, Hitachi) equipped with super EDS (Ultim Max, Oxford). The electrical resistances of the deposited iron-oxide and iron-nitride films were measured using a SEM (FEI Company Quanta 3D) equipped with four nano-manipulators (Klindiek, MM3A EM). Four nano-manipulators with tungsten tips were installed in a sample chamber to make electrical contact with the

individual fibers. The I-V curves were measured using a semiconductor device analyzer (Agilent Technologies, B1500A) employing a four-electrode method.

Cross-sectional images of the catalysts were obtained using electron probe microanalysis (EPMA). The cross-section of the electrodes was exposed by mechanically polishing the specimen prepared by embedding the electrodes in a room-temperature curing epoxy. Thin cross-sectional samples for TEM analysis were prepared using a focused ion beam (FIB) and SEM (Ethos NX5000, Hitachi). A focused beam of gallium ions was used for milling. After milling, a micromanipulator needle was used to transfer the thin specimen to the FIB transmission electron microscope (TEM) grid. Cross-sectional images were obtained using high-resolution TEM (Talos, Field emission Inc., Thermo Scientific).

2.3. PEMWE cell preparation and testing

The MEA was fabricated by placing an anode and cathode on each side of a Nafion 212 membrane (50 μm thickness, DuPont Co.). The cathode was prepared by spray-coating Pt/C catalysts (46.2 wt% Pt, Tanaka Kikinzoku group) with Nafion ionomer on a carbon-based gas diffusion layer (39 BCE, SGL group, 325 \pm 25 μm thickness, 5% PTFE) with a Pt loading of 0.2 mg/cm². A Nafion membrane was sandwiched between the prepared cathode and anode. Teflon gaskets with thicknesses of 250 μm were placed on each side of the Nafion membrane. The assembly was then hot-pressed for 1 min at 120 °C at a pressure of 2.7 MPa. The prepared MEA was placed between two current-collector plates with a serpentine flow channel. A carbon-based plate was used as the cathode current collector, whereas a titanium-based plate was used on the anode side. In the water electrolysis experiments, the cell temperature was maintained at 80 °C with a flow of preheated DI water on the anode (15 mL/min), and electrochemical analysis of the PEMWEs was conducted using a potentiostat (HCP-803, Biologics Ltd.). Linear sweep voltammetry was performed three times with different electrodes, and the average values are reported in this study. Electrochemical impedance spectroscopy (EIS) was performed at an applied cell voltage of 2.0 V_{cell} with an AC frequency ranging from 50 kHz to 100 mHz. In the experiments investigating the importance of the ion-conducting membrane and catalyst interface on the PEMEC

performance, the EIROF on the outermost layers of the Ti PTL, through which the membrane–catalyst interface is formed, was intentionally removed by polishing with an aluminum-oxide lapping film. The degree of surface ablation was maintained at \approx 5 μm by monitoring the thickness of the Ti PTL with a digital thickness gauge during polishing.

3. Results and discussion

3.1. Preparation and characterization of the iron-nitride nanostructure on Ti PTL

There are two main approaches to fabricate the catalyst layers in MEAs: deposition of the catalyst on the membrane or onto the PTLs [22]. The former approach is called the catalyst-coated membrane (CCM) method (Fig. 1a), in which catalysts are directly deposited on the electrolyte membrane using various methods such as spray coating, slot die coating, inkjet printing, or decal transfer. The second method, that is, direct deposition of the catalysts directly onto the PTLs, which transfer electrons from the current collector to the catalyst layers and facilitate the mass transport of reactants and products to the catalyst layer (Fig. 1b). Recently, Mo et al. investigated the spatial distribution of the OER reactivity over the catalyst layers by introducing a transparent and reaction-visible PEMWE [23]. It was observed that oxygen bubbles were not generated uniformly over the catalyst layers but were produced in abundance at the catalyst layers interfacing the Ti PTL. It was speculated that the electrical resistivity throughout the oxide catalysts was too high to activate the catalyst, which was far from the Ti PTL; therefore, the large in-plane ohmic loss could mainly account for the non-uniform activation of the OER electrode. Although the actual ohmic drop over the catalyst layer should be carefully quantified considering the electrical resistivity and conducting distance, the ohmic loss can be minimized by placing the catalyst directly on the Ti PTL to enhance catalyst utilization. In this respect, electrodeposition is a promising method to directly deposit the iridium catalysts on the PTL in a controlled manner (Fig. 1c). In this study, a thin iridium-oxide layer was placed on the earth-abundant iron-nitride nanostructure to enhance the utilization of the iridium catalysts and to replace the platinum protective layer with inexpensive transition metals in the PEMWE (Fig. 1d).

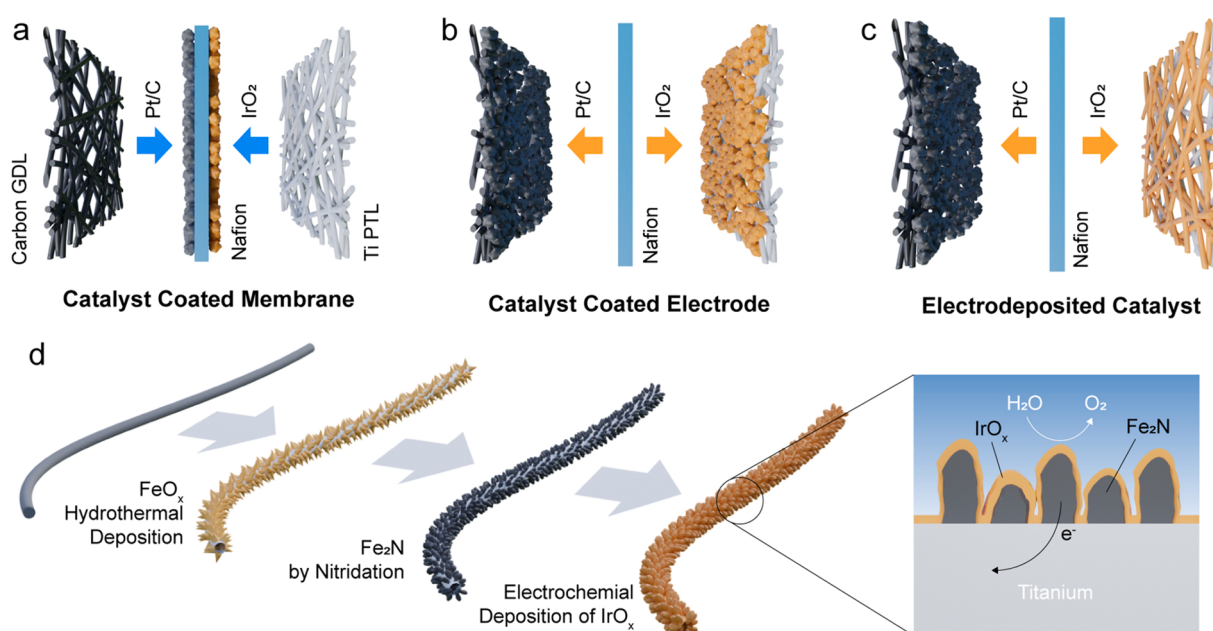


Fig. 1. Preparation of iron nitride-iridium oxide core-shell-structured electrodes for water electrolyzer. (a) Conventional catalyst-coated membrane electrode assembly for water electrolyzer. (b) Catalyst-coated electrode configuration for the preparation of the MEA. (c) Electrodeposition of iridium oxide on Ti PTL for the preparation of the MEA. (d) Fabrication of iron nitride-iridium oxide core-shell-structured Ti PTL.

To prepare the iron-nitride-coated Ti PTL, iron oxide nanorods were first deposited on the Ti PTL by the hydrothermal method [24,25]. The surface of the titanium PTL became yellow after the reaction, indicating the deposition of iron oxide over the surfaces (Fig. S1). SEM analysis revealed that iron-oxide nanorods with a width of $\approx 40\text{--}80\text{ nm}$ and length of $\approx 400\text{--}600\text{ nm}$ were deposited homogeneously on the surface of the Ti fibers by hydrothermal reaction (Fig. 2 a,b). The XRD analysis revealed that the iron-oxide nanorods consisted of an FeO wüstite structure and Fe₃O₄ magnetite structure (Fig. 2c). However, owing to the low electrical conductivity of oxide materials, it can be presumed that the iron-oxide-nanorod-decorated Ti PTL is inappropriate for water electrolysis with large operational current densities. Therefore, to enhance electrical conductivity, iron oxide was converted to iron nitride. The nitridation of iron oxide was carried out by annealing the oxide at a temperature controlled between 400 and 500 °C under an NH₃ atmosphere [26]. When nitridation was performed at 400 °C under NH₃, the XRD pattern indicated a decrease in Fe₃O₄, and the (111) peak of wüstite Fe_{1-x}O at 36.3° shifted to 36.0° (Fig. 2 d). The XRD was taken without any surface treatment after the annealing, e.g. Ar⁺ etching process to remove surface oxides (see below discussion on XPS analysis). The weak reflection at $2\theta = 36.0^\circ$ was indexed to the (111) peak of wüstite-like iron oxynitride (Fe_{1-x}O_yN_{1-y}), suggesting that partial nitridation of iron-oxide occurred [27,28]. SEM analysis also revealed that the morphology of iron oxide changed as the nitridation reaction occurred. Iron-oxide nanorods with a straight needle-like morphology agglomerated and became rounded particles after nitridation at 400 °C, as shown in Fig. S2. As the nitridation temperature was increased to 450 °C, the peak at $\approx 36.0^\circ$ disappeared, and a peak located at 43.0°, corresponding to the (101) plane of Fe₂N (PDF# 02-1206), emerged, signifying the complete conversion of oxides to nitrides. The Fe₂N nanostructure consist of Fe₂N nanoparticles produced on the Ti PTL were confirmed by SEM analysis (Fig. 2 e,f). In addition, the yellow iron-oxide film became black, suggesting that a successful phase transition of iron oxide to iron nitride occurred at 450 °C (Fig. S1).

When the nitridation temperature was increased to 500 °C, the XRD peaks at 56.8° and 67.9°, which correspond to the (102) and (110) planes of the Fe₂N, respectively, were more distinctly developed, suggesting that the crystallinity of the Fe₂N phase increased. However, the SEM analysis revealed that the Fe₂N particles were more significantly agglomerated while the underneath Ti surface was exposed. The agglomeration of the Fe₂N particles was more obvious when the annealing temperature was increased to 550 °C (Fig. S3). As the severe

agglomeration of particles results in a decrease in the specific surface area of the electrode, the nitridation temperature was fixed at 450 °C to preserve the large surface area of the Fe₂N core, which serves as an effective support for active water-oxidation catalysts, that is, iridium oxide.

The increased conductivity of iron oxide owing to nitridation was confirmed by four-point probe measurements (Fig. S4). For the bare Ti PTL, the electronic resistance between the two tungsten tips, 10 μm apart, was measured as 28.8 mΩ. By approximating the diameter of the Ti fiber as 20 μm, the resistivity of the bare Ti PTL was calculated to be $9.0 \times 10^{-7}\text{ }\Omega\text{ m}$. The difference in the resistivity between the Ti PTL obtained using a four-point probe measurement and the reported bulk Ti resistivity ($4.2\text{--}4.7 \times 10^{-7}\text{ }\Omega\text{ m}$) is less than an order of magnitude. This implies that the native oxide was not substantially developed on the surface of the Ti PTL, and the four-point measurement can be used to estimate the resistance of individual fibers [29,30]. When the four-point probe measurement was applied to a FeO_x-coated Ti fiber, the resistance was over the detection limit of the analyzer, and the insulating FeO_x layers prevented practical current flow at the Ti PTL surfaces. However, after the nitridation process, the resistance of the surface layer was reduced to 3.52 kΩ. It is noteworthy that our group previously measured the electrical resistance of the EIROF-coated Ti PTL fiber as 474 kΩ with the same measurement method, indicating that the electrical resistance of the Fe₂N layer is two orders of magnitude lower than that of the EIROF [12]. Considering the notably higher electric conductivity of the Fe₂N compared with that of the EIROF, it was concluded that the Fe₂N is an effective catalyst support for the EIROF, providing a large active surface area and improving the catalyst utilization with practical electron transport to the EIROF film.

The chemical states of the iron and nitrogen atoms in iron nitride were analyzed using XPS. The high-resolution Fe 2p XPS spectrum of iron nitride showed that the surfaces mainly consist of Fe(III) species, as indicated by the Fe 2p_{3/2} and Fe 2p_{1/2} peaks at 711.2 and 724.7 eV, respectively (Fig. 2g) [31]. In the analysis, high-BE surface peaks were used to fit the asymmetric peak of Fe 2p, and the peaks at 718.5 and 733.3 eV were assigned to the Fe satellite peaks [32]. This result suggests that the surface of the Fe₂N was partially oxidized by atmospheric oxygen after nitridation. However, the surface native-oxide on the Fe₂N can simply be removed by Ar⁺ ion irradiation [33]. After the ion-etching reaction, the XPS peaks which correspond to Fe(0) (706.8 and 720.0 eV), and peaks corresponds to Fe(0) (708.6 and 722.3 eV) emerged. The N 1 s signal in the XPS spectrum of Fe₂N (397.3–397.6 eV)

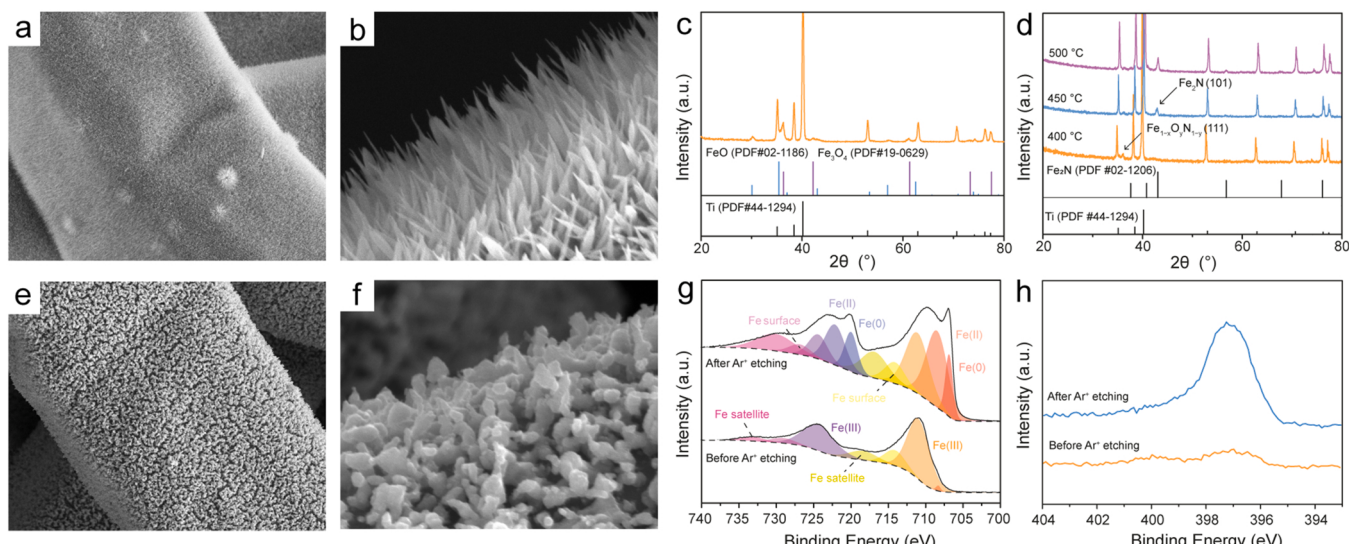


Fig. 2. Characterization of Fe₂N nanostructure on Ti PTL. (a-b) SEM image of iron-oxide nanorods on Ti PTL. (c,d) XRD spectra of the (c) iron-oxide nanorods and (d) Fe₂N nanostructure. (e,f) SEM image of Fe₂N nanostructure on Ti PTL. (g) Fe 2p XPS spectra and (h) N 1s XPS spectra of Fe₂N nanostructure.

also increased after the ion-etching process and removal of the surface native oxide indicating the successful formation of the Fe₂N through FeO_x nitridation treatment (Fig. 2h) [34].

3.2. Formation of the electrodeposited iridium-oxide film (EIROF) on Ti PTL

Iridium oxide was fabricated on the prepared Fe₂N nanostructure via electrodeposition. The electroplating solution contained stable iridium-oxide colloids formed by mixing IrCl₄, H₂O₂, oxalate, and carbonate in an aqueous solvent [21]. The iridium-oxide film was deposited by applying a constant potential of 0.7 V_{SCE}. On the FeO_x-decorated Ti PTL, electrodeposition was impractical, with an insignificant deposition current detected at the insulating FeO_x electrode (Fig. S5). However, IrO_x was obviously deposited on the surfaces of the bare Ti PTL and the Fe₂N @ Ti PTL, as the electrode was colored black upon electrodeposition of IrO_x with a relatively high oxidative current during the electrodeposition step (Fig. S6). The amount of deposited Ir deposited was controlled by varying the electrodeposition time (t_{dep}) from 1 to 10 min.

The surface morphologies of the EIROF on the bare Ti PTL with different t_{dep} values are shown in Fig. 3. At a short t_{dep} of 1 min, a thin EIROF comprising heterogeneously deposited spherical Ir particles covered the bare Ti PTL (Fig. 3a). EDS line-scanning also confirmed the formation of EIROF on the Ti fibers (Fig. S7). As t_{dep} increased to 3 and 5 min, the Ti surface acquired a thicker EIROF layer and became rougher (Fig. 3.b, and c). In addition, the EDS intensity of Ti weakened, whereas that of Ir intensified as the EIROF thickened with a longer deposition time (Fig. S7). However, as t_{dep} was increased to 10 min, cracks formed in thicker EIROF (Fig. 3d). It is speculated that the strain and volume change induced by dehydration of iridium oxide film after drying the electrode caused cracks in the thick EIROF. The morphology of the EIROF coated on the Fe₂N/Ti PTL was also investigated using SEM. As shown in Fig. 3e, the Fe₂N nanostructure remained intact, maintaining the pore structure between the Fe₂N particles when the EIROF was electrodeposited for 1 min. By increasing t_{dep} to 3 and 5 min, the EIROF grew uniformly on the Fe₂N nanostructure, resulting in a narrower spacing between the Fe₂N particles (Fig. 3f and g). Eventually, when t_{dep} was increased to 10 min, a thick EIROF filled the nanogap between the Fe₂N particles, and cracks developed at the surface of the EIROF, as similarly observed in the EIROF formed on the bare Ti PTL with a t_{dep} of 10 min (Fig. 3h).

The gradual increase in the Ir loading with increasing t_{dep} was quantified by conducting ICP-AES measurements (Fig. S8). As t_{dep} increased from 1 to 10 min, the Ir loading of the EIROFs increased from 22 to 144 µg/cm², respectively, for the bare Ti PTL. When the EIROFs were deposited on the Fe₂N-coated Ti PTL, the Ir loading slightly increased compared with that of the bare Ti PTL for the same t_{dep} . Specifically, the Ir loadings on the Fe₂N-coated Ti PTL were 36 and 165 µg/cm² for t_{dep} values of 1 and 10 min, respectively. It has been suggested that the oxidative EIROF deposition involves the electrophoretic deposition of iridium oxide colloids which present in the electroplating solution including side reactions, e.g. oxygen evolution reaction or surface oxidation [21]. It is also suspected that the high surface area of the Fe₂N nanostructure provides more sites for electrodeposition, resulting in higher Ir loadings at identical t_{dep} values. The oxidation state of Ir in the EIROF was analyzed using XPS. As shown in Fig. S9, two asymmetric Ir 4 f peaks were observed at approximately 65.1 (4 f_{5/2}) and 62.2 eV (4 f_{7/2}). The broadness of the peaks suggests that the electrodeposited iridium oxide has mixed Ir valence states [35]. The peaks were deconvoluted, revealing Ir(IV) peaks at 65.10 (4 f_{5/2}) and 62.10 eV (4 f_{7/2}), Ir(III) peaks at 66.55 (4 f_{5/2}) and 63.55 eV (4 f_{7/2}), and their respective satellite peaks at higher binding energies.

The deposition of Ir on the Ti PTL or the Fe₂N-coated Ti PTL was also confirmed by measuring the Ir(III)/(IV) and Ir(IV)/Ir(V) redox couples of the EIROF in the cyclic voltammograms (CVs). The Ir redox transition was observed in the potential window of 0.4–1.2 V_{RHE} without interference of the water oxidation reaction at pH 7 phosphate buffered solution (Fig. S10). The peaks at approximately 0.8 and 1.2 V_{RHE} correspond to the Ir(III)/(IV) and Ir(IV)/(V) redox couples, respectively, of the EIROF formed on the substrate [36]. In addition, the increased redox current for Ir(III)/(IV) and Ir(IV)/(V) with increasing t_{dep} clearly shows that the amount of active iridium species in the EIROF increases with t_{dep} .

Interestingly, the intensities of the Ir(III)/(IV) and Ir(IV)/(V) redox peaks of the EIROF and their dependence on t_{dep} were different for the bare Ti PTL and the Fe₂N-coated Ti PTL electrodes. For the EIROF on the Fe₂N-coated Ti PTL, the peak currents of both Ir(III)/(IV) and Ir(IV)/(V) constantly increased with t_{dep} . However, the intensity of the Ir(IV)/(V) peak increased more distinctly than that of the Ir(III)/(IV) peak with increasing t_{dep} at the EIROF on the bare Ti PTL, resulting in the differences in peak intensity between Ir(IV)/(V) and Ir(III)/(IV) peak. Ilyukhina et al. reported that the ratio between Ir(III)/(IV) and Ir(IV)/(V)

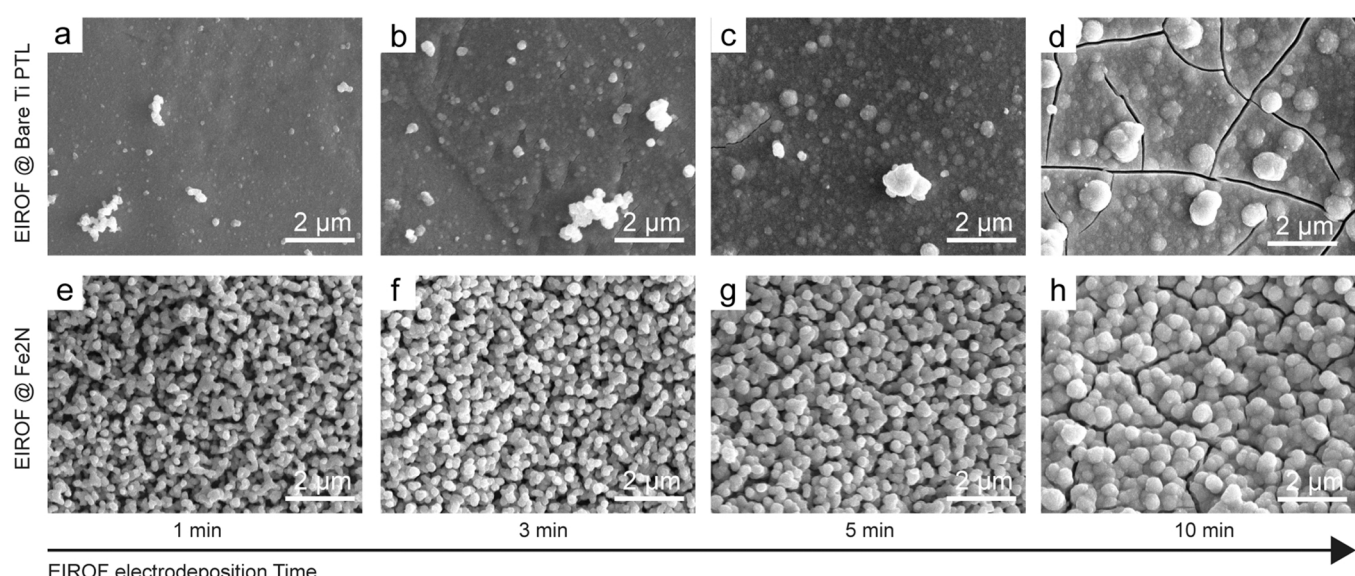


Fig. 3. Morphology of the EIROF. (a-d) Morphology of EIROF on Ti PTLs with different electrodeposition times. (e,f) Morphology of EIROF on Fe₂N-coated Ti PTLs with different electrodeposition times.

redox peak depends on the thickness of EIROF. They showed that the Ir(III)/(IV) and Ir(IV)/(V) peaks are symmetric when EIROF is thin, while it becomes asymmetric with thick EIROF [37]. They explained that Ir(III)/(IV) redox reaction is inhibited when the EIROF is thicker than space-charge region. However, the conductivity of the film is enhanced with high applied potential, enough for the redox reaction to occur leading to a so-called block-release behavior; the Ir(III)/(IV) redox reaction is blocked at the low applied potential and released at the high potentials where iridium oxide film becomes conductive. Thus, the peak intensity between Ir(IV)/(V) and Ir(III)/Ir(IV) becomes asymmetric with thick EIROF [37]. This implies that the EIROF is thicker on the bare Ti PTL, even with a lower amount of IrO_x, than the film on its Fe₂N-coated counterpart.

The thickness of the EIROF was analyzed and confirmed by cross-sectioning the sample using a FIB. High-angle annular dark-field scanning-transmission electron microscopy (HAADF-STEM) analysis of a thin cross-sectioned sample shows the planar EIROF deposited on a Ti PTL (Fig. 4a). EDS elemental mapping analysis shows that the thickness of the EIROF with $t_{dep} = 5$ min is 103 ± 6 nm (Fig. 4b). HAADF-STEM image of the Fe₂N @ EIROF shows Fe₂N nanoparticles deposited on Ti PTL with the EIROF coated on them. The EIROF appears brighter than Fe₂N, due to the higher atomic number of Ir compared to that of Fe (Z-contrast) (Fig. 4c). EDS elemental mapping analysis shows that the thickness of the EIROF on Fe₂N nanoparticles is 35 ± 5 nm, much thinner than that of the bare Ti PTL. Also, the core-shell structure of the EIROF-coated Fe₂N nanoparticles is clearly visible (Fig. 4d). The $\approx 60\%$ thinner EIROF on the Fe₂N nanoparticles, as observed using electron microscopy, strongly support the CV results, which revealed a lower electrical resistance compared with that of the EIROF on the bare Ti PTL.

3.3. PEMWE performances

The OER activity of the prepared electrodes was further evaluated in an MEA configuration. The MEA was prepared by hot-pressing a stack of Pt/C spray-coated carbon paper (cathode), Nafion 212, and the EIROF-coated Ti PTLs (anode). The prepared MEA was placed between the two current collectors with a serpentine flow field. The performance of the prepared PEMWE was evaluated at 80 °C by supplying DI water only at the anode side. The polarization curves of the PEMWEs with the EIROF-coated Ti PTL without the Fe₂N nanostructure are shown in Fig. 5a. With

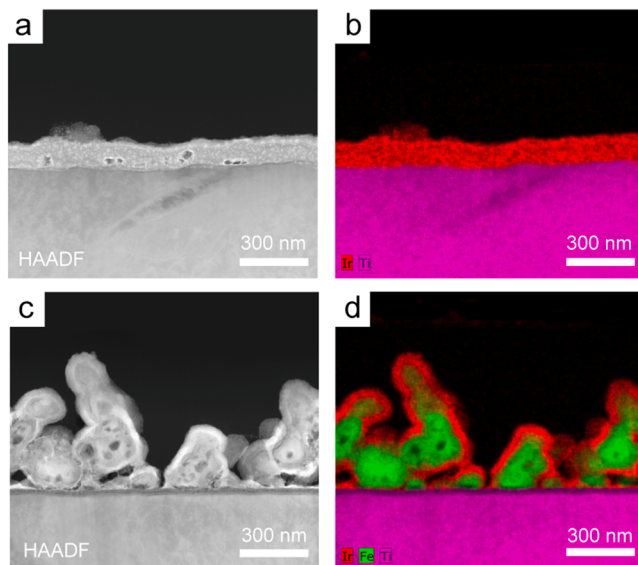


Fig. 4. Cross-section of the EIROF. (a) High-angle annular dark-field scanning-transmission electron microscopy (HAADF) image and (b) EDS image of the EIROF on bare titanium surface. (c) HAADF image and (d) EDS image of the EIROF on Fe₂N-coated titanium surface.

an increase in t_{dep} , a gradual increase in PEMWE performance was observed until t_{dep} reached 5 min. The current density of the PEMWE increased from 0.69 A/cm^2 ($t_{dep} = 1$ min) to 2.16 A/cm^2 ($t_{dep} = 5$ min) at an applied cell voltage of 1.9 V_{cell} . We believe that the current density increased as the EIROF with rougher surface was deposited on the Ti PTL with an increase in t_{dep} as shown in Fig. 3. However, no significant improvement in the PEMWE performance was observed for the EIROF with $t_{dep} = 10$ min; the current density reached 2.27 A/cm^2 at 1.9 V_{cell} , indicating that the inner Ir atoms inside the thick EIROF did not efficiently participate in water oxidation reaction. Importantly, when the EIROFs deposited on the Fe₂N-coated Ti PTL were used in the device, the PEMWE performance was significantly enhanced compared with the performance of the PEMWE incorporating the Ti PTL without the Fe₂N layer (Fig. 5b). As shown in Fig. 5c, even the EIROF deposited on the Fe₂N nanostructure for 1 min exhibited a current density of 3.62 A/cm^2 at 1.9 V_{cell} , which is five-fold higher than that of the EIROF deposited on the bare Ti PTL for 1 min. The current density of the Fe₂N @ EIROF on the Ti PTL reached 4.50 A/cm^2 at 1.9 V_{cell} by increasing t_{dep} to 3 min, which is approximately three-fold higher than that of the EIROF on the bare Ti PTL ($t_{dep} = 3$ min). However, furthering increasing t_{dep} beyond 3 min barely increased the performance of the PEMWEs based on the Fe₂N @ EIROF. It is interesting that the current density plateaued with shorter electrodeposition time than that of the EIROF-Ti PTL. We suspect that as the Fe₂N nanostructures has already high surface area and roughness, the OER activity was less affected by the morphology of the EIROF itself. It plateaued when Fe₂N is fully covered by the EIROF, while the activity of the EIROF-Ti PTL was greatly affected by the surface roughness of the EIROF on bare Ti PTL. After $t_{dep} = 3$ min, the current density marginally increased with t_{dep} from 3 to 10 min and even decreased at voltages greater than 1.9 V_{cell} . As shown in Fig. 3, the spacing between the EIROF coated Fe₂N nanoparticles narrows as t_{dep} increases, so the ineffective mass transport of water and produced oxygen bubbles at the narrower pore might prevent a further increase in PEMWE performance when $t_{dep} > 3$ min.

A complementary EIS analysis was conducted to explain the performance of the PEMWEs. The spectra were analyzed using an equivalent electrical circuit model, as depicted in Fig. S11a. The equivalent circuit includes the ohmic resistance (R_Ω) and two kinetic resistances, i.e., charge transfer resistance (R_{ct}) and mass transfer resistance (R_{mt}), connected in parallel with the constant phase elements (CPEs) [38,39]. The R_Ω can be determined by the high-frequency x-axis intercept in the Nyquist plot. The R_{ct} is attributed to the charge transfer of the rate-determining step of the OER and R_{mt} to the mass-transport phenomena, respectively [40]. The R_{ct} can be determined by the radius of the semi-circle at high frequency region, and R_{mt} by the radius of the semi-circle at low frequency region. The Nyquist plots of the EIROF-Ti PTLs are shown in Fig. S11b. In the case of the Ti PTLs with a t_{dep} of 1 min or 3 min, the spectra cannot be fitted with the proposed equivalent circuit model owing to the abnormal behavior in the high-frequency region. The occurrence of this abnormality, especially in the low-performance PEMWEs, is interesting, but because the origin of the impedance feature in the high-frequency region is obscure, a fitting analysis of the EIROF-Ti PTLs with t_{dep} values of 1 min and 3 min was not conducted. When more Ir was deposited onto the Ti PTL, Nyquist plots consisting of two semicircles can be observed and fitted with the proposed equivalent-circuit model. The fitting results for the EIROF-Ti PTLs are shown in Fig. S11c and d and are summarized in Table S1.

In contrast with those of the EIROF-Ti PTLs, the Nyquist plots of the Fe₂N @ EIROF-Ti PTLs consisted of two semicircles, even with a short t_{dep} of 1 min. The positive effect of the Fe₂N support on the PEMWE performance is evident in the Nyquist plot by the reduced R_{ct} and R_Ω values. The fitting results for the Fe₂N @ EIROF-Ti PTLs are shown in Fig. S11e-h and are summarized in Table S1. The average R_{ct} of the Fe₂N @ EIROF-Ti PTLs was measured to be $3.1 \text{ m}\Omega \text{ cm}^2$, which is much lower than those of the EIROF-Ti PTLs (i.e., 7.9 and $7.0 \text{ m}\Omega \text{ cm}^2$ for t_{dep} values of 5 and 10 min, respectively). The decrease in R_{ct} suggests that

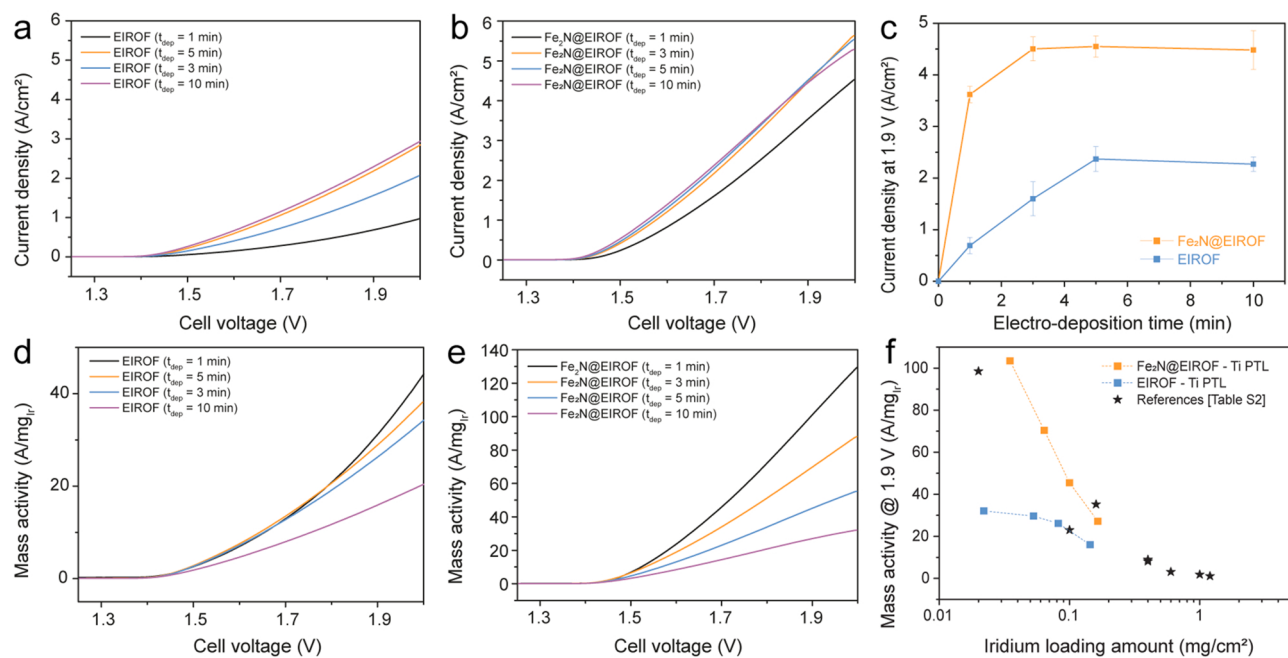


Fig. 5. Performance of PEMWEs with prepared electrodes. (a) PEMWE performances with EIROFs on bare Ti PTLs. (b) PEMWE performances with the EIROF on Fe₂N-coated Ti PTLs. (c) Comparison of current density with applied cell voltage of 1.9 V. Ir-based mass activity of (d) EIROFs on bare Ti PTLs, and (e) EIROFs on Fe₂N-coated Ti PTLs.

the OER occurs more effectively in the PEMWE. As shown in Fig. 4, a much thinner iridium oxide layer can be prepared on the Fe₂N nanostructure with the same t_{dep} . As the Ir active sites inside the thick EIROF cannot effectively participate in OER, thin EIROF with a larger surface area on the Fe₂N nanostructures could enhance Ir atomic efficiency leading to higher Ir mass activity. As a result, the Fe₂N @ EIROF exhibits a higher current density compared to that of the EIROF on Ti PTL at the same applied potential. As the resistance of PEIS is normalized by the geometrical surface area (electrode area), the higher current density of the Fe₂N @ EIROF due to the higher actual surface area results in the lower apparent R_{ct} compared to that of the EIROF on Ti PTL. In addition, a decrease in the R_{Ω} can also be observed. Similarly, the average R_{Ω} of the Fe₂N @ EIROF-Ti PTLs was 71.6 mΩ cm², which is lower than that of the EIROF-Ti PTLs (i.e., 114.6 and 119.5 mΩ cm² for t_{dep} values of 5 min and 10 min, respectively). Furthermore, by introducing a porous structure on the catalyst layers, mass transport in the PEMWEs was greatly enhanced. The R_{mt} of the Fe₂N @ EIROF ($t_{dep} = 1$ min) was the lowest (i.e., 5.5 mΩ cm²). However, as the EIROF on Fe₂N thickens, the EIROF blocks the porous structure of the Fe₂N nanoarrays, causing R_{mt} to gradually increase to 12.4 mΩ cm², which is comparable to that of the EIROF-Ti PTL (11.0 mΩ cm², $t_{dep} = 10$ min).

The mass activities of Ir on the bare Ti PTLs are shown in Fig. 5d, which were calculated by dividing the current densities by the Ir loading amounts. The EIROFs deposited on the Ti PTLs for 1–5 min showed similar mass activities when the applied voltage was below 1.75 V_{cell}, while the mass activities decreased at a higher applied voltage with increasing t_{dep} . This decrease in mass activity at a high applied voltage is believed to be caused by the mass transport limitation at the electrode with higher Ir loading. When t_{dep} was increased to 10 min, a drastic decrease in the Ir mass activity was observed, suggesting that the inner IrO_x nanoparticles of the thick EIROFs do not efficiently participate in the OER reactions. Thus, it is expected that substituting the inner IrO_x with conductive Fe₂N can greatly enhance the Ir mass activity. As expected, the EIROFs on the Fe₂N-coated Ti PTL showed higher mass activities than the EIROFs on the Ti PTL (Fig. 5e). Fe₂N @ EIROF ($t_{dep} = 1$ min) showed a high mass activity of 103.4 A/mg_{Ir} at 1.9 V, which is 3.2-fold higher than that of the EIROF-Ti PTLs ($t_{dep} = 1$ min). The Ir

mass activities of the EIROF and the Fe₂N @ EIROF-Ti PTLs on the PEMWEs fabricated in this study and those of previously reported Ir-based PEMWEs are summarized in Fig. 5f and Table S2, showing that the TMN-based core–shell approach is a promising way to enhance the Ir mass activity, reducing the required Ir loading in the PEMWEs. However, the mass activity decreased more drastically than that of the EIROF-Ti PTLs with increasing t_{dep} , which implies that the electrolyzer performance becomes more dependent on the mass-transport resistance rather than the OER charge-transfer resistance. As shown in Fig. S12, the ratio between R_{lf} and R_{hf} for the Fe₂N @ EIROF-Ti PTLs was much higher than that for the EIROF-Ti PTLs. In addition, the increase in R_{lf}/R_{hf} with t_{dep} suggests that the performance of the PEMWEs is mainly limited by the mass-transport resistance.

Finally, the stability of the PEMWEs employing the Fe₂N-layered Ti PTL electrode was investigated. The stability of the PEMWE electrode is a critical feature for economical, green hydrogen production. Platinum group metals (PGMs) such as Pt, Au, and Ir are widely used as protective layers for PTLs owing to their robustness under harsh oxidative conditions of PEMWEs. However, the use of a substantial amount of PGMs at the anode is one of the reasons preventing the rapid deployment of PEMWEs in the field. Herein, the performance and stability of the PEMWEs using the EIROF@Fe₂N-Ti PTL anode were compared with those of a Pt-coated Ti PTL to evaluate the feasibility of using TMNs instead of PGMs in the anode of PEMWEs. In this context, the Fe₂N @ EIROF-Ti PTL with a t_{dep} of 5 min was selected as a representative electrode and compared with the Pt@EIROF-Ti PTL, which we previously optimized [12]. The EIROF was also electrodeposited for 5 min on the Pt-coated Ti PTL to yield a similar amount of the EIROF. The morphology of the Pt@EIROF-Ti PTL is shown in Fig S13. The XRD analysis showed that the metallic Pt was electrodeposited on Ti PTL (Fig. S14). The peaks for EIROF were not detected as the EIROF is known to be amorphous or has very low crystallinity [41]. But the presence of both Pt and Ir on the Ti PTL was clearly shown by EDS analysis (Table S3). The performance and durability of the PEMWEs were evaluated using a dynamic operation condition [42]. Specifically, a cycled square-wave galvanic input was applied to the PEMWEs, which involved alternating the current density between 0.1 and 2.0 A/cm² for 6 h, for a

total 120 h, to observe if the electrode presents any rapid and initial degradation by the catalyst corrosion. The performance and cell-voltage trends of the PEMWEs during the durability test are shown in Fig. 6.

At a low current density of 0.1 A/cm^2 , the degradation rate was similar: $340 \mu\text{V/h}$ and $334 \mu\text{V/h}$ for the $\text{Fe}_2\text{N} @ \text{EIROF-Ti PTL}$ and the $\text{Pt} @ \text{EIROF-Ti PTL}$, respectively (Fig. 6a and c). Interestingly, at a high applied current density of 2.0 A/cm^2 , the degradation rate of the PEMWE containing $\text{Pt} @ \text{EIROF-Ti PTL}$ was $788 \mu\text{V/h}$, which is higher than that of the $\text{Fe}_2\text{N} @ \text{EIROF-Ti PTL}$ ($368 \mu\text{V/h}$). The LSVs after the stability test also showed that the performance of the PEMWE composed of the $\text{Pt} @ \text{EIROF-Ti PTL}$ was more degraded than that of the PEMWE containing the $\text{Fe}_2\text{N} @ \text{EIROF-Ti PTL}$ (Fig. 6b and d). However, we would conclude that the $\text{EIROF-Fe}_2\text{N-Ti PTL}$ anode is more durable than the $\text{Pt} @ \text{EIROF-Ti PTL}$ anode from this particular result. The performance of the high-current-density region of the PEMWE is affected not only by catalyst degradation but also mass transportation and ohmic resistance.

We suspect that the poor stability of the $\text{Pt} @ \text{EIROF-Ti PTL}$ was mainly caused by the chemical instability of the Nafion 212 membrane toward peroxide, possibly produced by hydrogen crossover and the presence of Pt on the anode [43,44]. Thus, the stability of the PEMWEs was investigated with a more robust Nafion 115 membrane (Fig. S15). With a low applied current density of 0.1 A/cm^2 , the degradation rates of PEMWEs incorporating Nafion 115 were similar to those containing Nafion 212, that is, $309 \mu\text{V/h}$ and $322 \mu\text{V/h}$ for the $\text{Fe}_2\text{N} @ \text{EIROF-Ti PTL}$ and the $\text{Pt} @ \text{EIROF-Ti PTL}$, respectively (Fig. S15a and c). However, at a high applied current density of 2.0 A/cm^2 , the degradation rate of the $\text{Pt} @ \text{EIROF-Ti PTL}$ decreased to $209 \mu\text{V/h}$, which is much lower than the $788 \mu\text{V/h}$ degradation rate of its PEMWE counterpart containing the Nafion 212 membrane. Compared with the $\text{Pt} @ \text{EIROF-Ti PTL}$, the $\text{Fe}_2\text{N} @ \text{EIROF-Ti PTL}$ exhibited a higher degradation rate of $414 \mu\text{V/h}$. Although the Nafion-115-based $\text{Pt} @ \text{EIROF-Ti PTL}$ was more stable than the $\text{Fe}_2\text{N} @ \text{EIROF-Ti PTL}$, the LSVs acquired after the stability test revealed that the performance of the latter PEMWE was maintained (Fig. S15b and c). The morphology of $\text{Fe}_2\text{N} @ \text{EIROF}$ after the stability test was investigated by SEM analysis (Fig. S16). The structure of $\text{Fe}_2\text{N} @ \text{EIROF}$ directly interfacing with Nafion membrane was partially damaged possibly due to the hot-pressing procedure on MEA construction and disassemble process of MEA for the characterization (Fig. S16a). However, the nanostructures of the $\text{Fe}_2\text{N} @ \text{EIROF}$ that were not directly in contact with Nafion membrane remain intact

(Fig. S16b). EDS analysis showed that the Fe_2N nanoparticles were preserved on the electrode after long term stability test although some Fe leached out (Table S4). The durability test indicated that the $\text{Fe}_2\text{N} @ \text{EIROF-Ti PTL}$ served as a practical catalyst support for IrOx owing to the good surface protection provided by the thin layer of IrOx OER catalyst. In other words, TMN-based core-shell materials are effective for supporting Ir catalysts in PEMWEs, replacing Pt in the conventional PEMWE anode.

3.4. Investigation of the role of Nafion/catalyst interface on the PEMEC performance

It is of great interest that which spatial portion of the catalyst layer is the actual site of the electrochemical reactions site where the electrochemical reactions really occur, especially in the membrane electrode assembly [45]. In many of the studies on PEMWEs with CCM configurations, iridium-oxide catalysts are usually first dispersed in the solvent with an ionomer polymer binder, and the catalyst inks are deposited on the solid membrane. This results in catalyst layers in which the ionomer binder is homogeneously mixed with the catalysts. It has been suggested that the appropriate amount of ionomer is important for establishing the ion-conduction pathway between the iridium catalyst and Nafion membrane [46]. However, it should be noted that the PEMWE with the EIROF-coated Ti PTL shows good water-splitting performance, even though the proton-conducting ionomers were not applied on the surface of the EIROF. Therefore, we investigated the influence of the Nafion membrane on the catalyst layers of the PEMWE and whether the Nafion-catalyst contact is essential to obtaining high-performance PEMWEs.

The Ti PTLs used in this study had a thickness of $250 \mu\text{m}$ and consisted of several layers of Ti microfibers with diameters of $20\text{--}30 \mu\text{m}$ (Fig. S17). The spatial distribution of EIROF on the Ti PTL was analyzed using SEM-wavelength dispersive spectroscopy elemental mapping analysis. It can be seen that most of the Ir is deposited on the outer surface of the Ti PTL to a depth of $\approx 50 \mu\text{m}$, which corresponds to 1–2 layers of Ti microfibers (Fig. 7). The spatial distribution of the EIROF on $\text{Fe}_2\text{N} @ \text{Ti}$ was similar to that of the bare Ti PTL; Ir was only deposited on layers 1–2 of the Ti microfibers. When the EIROF-coated PTLs were assembled onto a Nafion membrane, two different interfacial contacts arose: the EIROF deposited on the outermost Ti fibers of the Ti PTL facing the Nafion membrane, denoted as $\text{EIROF}_{\text{Nafion}}$; and the EIROF

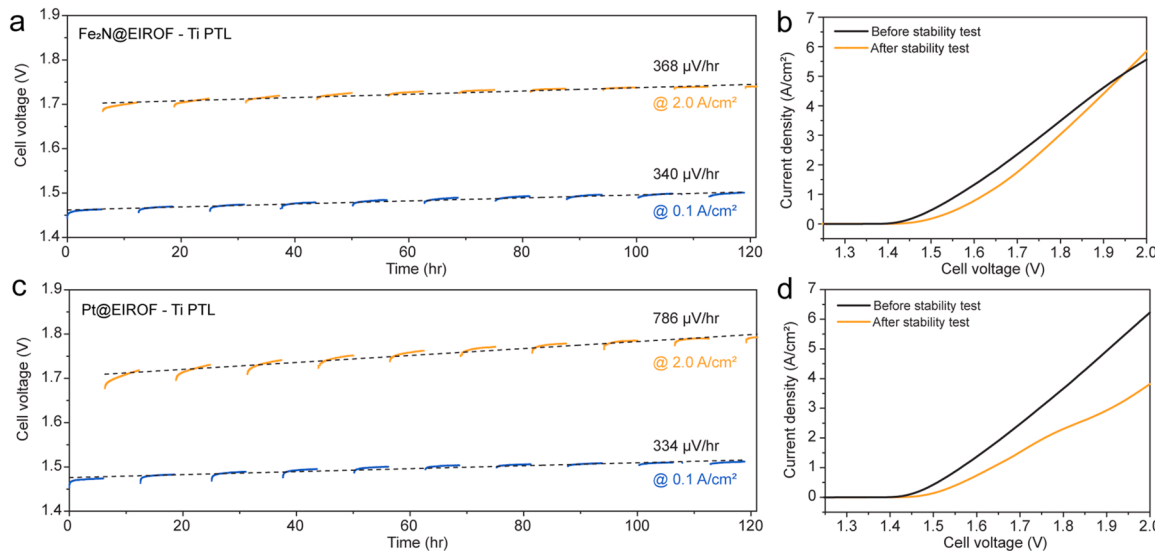


Fig. 6. Initial stability of PEMWEs with prepared electrodes. (a) Long-term PEMWE operation with the EIROF on Fe_2N -deposited Ti PTLs ($\text{Fe}_2\text{N} @ \text{EIROF-Ti PTL}$). (b) LSV of PEMWE with the $\text{Fe}_2\text{N} @ \text{EIROF-Ti PTL}$ before and after long-term operation. (c) Long-term PEMWE operation with the EIROF on Pt-deposited Ti PTLs ($\text{Pt} @ \text{EIROF-Ti PTL}$). (d) LSV of PEMWE with the $\text{Pt} @ \text{EIROF-Ti PTL}$ before and after long-term operation.

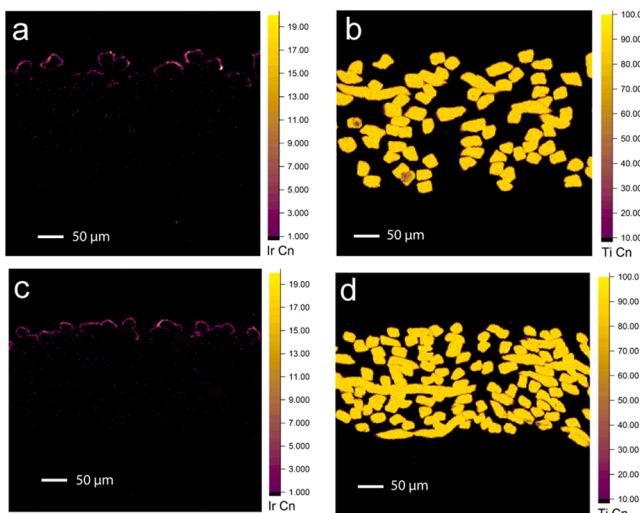


Fig. 7. Electron-probe microanalysis of the cross-section of iridium-coated Ti PTLs. (a) Ir and (b) Ti elemental mapping of the cross-section of the EIROF-coated Ti PTLs. (c) Ir and (d) Ti elemental mapping of EIROF on Fe_2N -coated Ti PTLs.

deposited inside the Ti PTL, facing DI water denoted as EIROF_{water}. If we assume that the catalysts in contact with the Nafion are active sites, EIROF_{Nafion} will presumably be the reaction site that dominates the overall PEMWE performance.

To investigate which interface governs catalyst utilization, we intentionally removed the EIROF film on the Ti PTL by mechanical polishing. If the EIROF_{Nafion} mainly accounts for the water oxidation reaction, it can be presumed that the performance of the PEMEC will be drastically reduced by removing the iridium oxides on the outermost layers of the Ti PTL, which contact the Nafion membrane (Fig. S18). The

degree of surface ablation was controlled by measuring the thickness of the Ti PTL using a digital thickness gauge during the polishing process. The thickness of the Ti PTL was measured at five points and then averaged. The change in thickness was controlled at $\approx 5 \mu\text{m}$. By polishing the EIROF-coated Ti electrode, the EIROF deposited on the outermost surface of the Ti PTL was removed, and a silvery Ti surface was revealed after polishing, as shown in Fig. S19. The distribution of Ir on the Ti PTL after polishing was analyzed using EPMA (Fig. 8a,b and c). It can be clearly seen that the EIROF was removed, and the underlying Ti surface was exposed on the outermost surface of the Ti PTL, while the EIROF on the second Ti fiber was intact. The performances of the abraded EIROF@Ti electrodes are shown in Fig. 8d. Interestingly, the PEMWE performance did not decrease, even though the EIROF in contact with Nafion was removed. This result suggests that the EIROF that adheres to the Nafion membrane does not affect the overall PEMWE performance. Instead, the EIROF deposited on the inner Ti fiber that does not contact the Nafion membrane dominates the overall PEMWE performance. It is generally believed that the presence of a Nafion ionomer is important for transporting protons from the catalyst layers to the Nafion membrane because DI water has a high ionic resistance. However, these results suggest that protons can be transported from the catalyst surface to the Nafion membrane, even if they are not in direct contact with Nafion. We assume that the increased ion concentration owing to the protons produced by the water-oxidation reaction can increase the ion conductivity of water between the catalyst layers and Nafion membranes. Thus, the PEMWEs can operate even if the Nafion ionomer is not applied to the surface of the EIROF-Ti PTLs.

The difference in the PEMWE performance following surface abrasion of the Fe_2N @ EIROF-Ti PTL is shown in Fig. 8e. Interestingly, a decrease in the current density was observed, suggesting that the outermost layer of the Fe_2N @ EIROF is active for OER, different from the EIROF-Ti PTLs. We assume that the difference in the behavior of the Fe_2N @ EIROF/Ti and the EIROF-Ti PTLs originates from the difference in the morphology of the catalyst layer. As the EIROF-Ti PTLs have dense

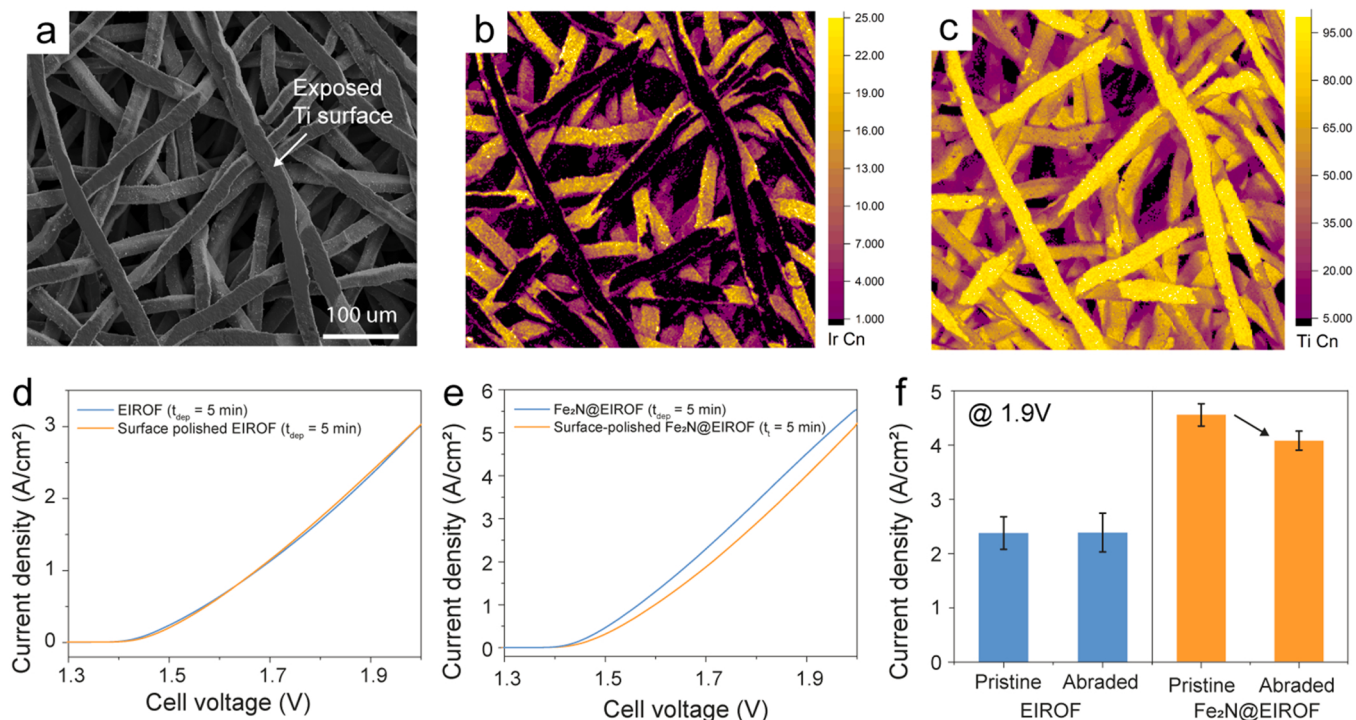


Fig. 8. Spatial distribution of iridium-oxide layers and their influence on the PEMWE performance. (a) Morphology of surface-polished iridium-oxide-coated Ti PTL. (b) Ir and (c) Ti distribution on the surface-polished electrode. (d) Electrolyzer performance after removing surface iridium-oxide layer on the Ti PTL. (e) Electrolyzer performance of the Ir- and Fe_2N -coated Ti PTL after removing the surface catalyst layer. (f) Differences in the current density after removing the surface catalyst layer.

planar Ir layers, it can be expected that there will be no gap between the EIROF_{Nafion} and the Nafion membrane when they come into contact. Although the Nafion membrane is hydrated with water molecules, the self-diffusion coefficient of water in hydrated Nafion is suggested to be two orders of magnitude smaller than that of bulk water [47,48]. As a result, when the Nafion membrane covers the surface of the EIROF, water transport to the active sites of the catalyst is limited, resulting in the low activity of the EIROF_{Nafion} (Fig. S20a). On the contrary, the EIROF on Fe₂N can participate in the OER because the Fe₂N nanostructure provides pores where water can transport (Fig. S20b). Therefore, by removing the outermost layer of the samples, the PEMWE current density decreased, whereas that of the EIROF/Ti did not change significantly (Fig. 8f). More detailed experimental and theoretical studies on the importance of the gap between OER catalysts and Nafion membranes are being conducted in our research group and will be presented in a future paper.

4. Conclusion

To develop an efficient and stable low-iridium-loaded anode for a PEMWE, the Fe₂N @ EIROF core–shell–nanostructure was fabricated on a Ti PTL. Fe₂N nanostructure was prepared on the Ti PTL by the hydrothermal deposition of FeO_x nanorods and a sequential nitridation process. On the prepared Fe₂N nanostructure, thin iridium-oxide layers of amount less than few tens $\mu\text{g}/\text{cm}^2$ were successfully deposited using the electrodeposition method. By using the unique Fe₂N @ EIROF core–shell structure, enhanced PEMWE performance and more than three-fold higher Ir mass activity can be achieved. Importantly, it was demonstrated that the EIROF directly facing the polymer membrane was actually inactive for water electrolysis without the Fe₂N support. By contrast, as the porous Fe₂N nanostructures provided ion and mass transport paths for water electrolysis, both the outermost and inner catalyst layers can be utilized with the Fe₂N @ EIROF electrodes. Finally, in a stability test of the PEMWEs, the electrode employing the Fe₂N @ EIROF anode demonstrated a stability comparable to that of the Pt@EIROF. This study clearly demonstrates that TMNs can be used as functional protective layers and catalyst supports instead of Pt for cost-effective PEMWEs.

CRediT authorship contribution statement

Hui-Yun Jeong: Conceptualization, Methodology, Investigation, Data curation, Formal analysis, Writing – original draft. **Jinho Oh:** Investigation, Data curation. **Gyu Seong Yi:** Validation, Visualization. **Hee-Young Park:** Resources. **Sung Ki Cho:** Resources. **Jong Hyun Jang:** Resources. **Sung Jong Yoo:** Funding acquisition, Project administration. **Hyun S. Park:** Writing – original draft, Funding acquisition, Supervision, Project administration.

Declaration of Competing Interest

There is no competing interest to be declared.

Data Availability

Data will be made available on request.

Acknowledgements

This work was supported by the Creative Materials Discovery Program through the National Research Foundation of Korea (NRF-2021M3D1A2051389), Ministry of Trade, Industry & Energy of Korea (MOTIE-20018989 and 20223030040220), and Korea Institute of Science and Technology (2E31871). This work was supported in part under the auspices of the U.S. Department of Energy by Lawrence Livermore National Laboratory under Contract DE-AC52-07NA27344.

Appendix A. Supporting information

Supplementary data associated with this article can be found in the online version at doi:10.1016/j.apcatb.2023.122596.

References

- [1] A. Buttler, H. Spliethoff, Current status of water electrolysis for energy storage, grid balancing and sector coupling via power-to-gas and power-to-liquids: a review, Renew. Sust. Energ. Rev. 82 (2018) 2440–2454, <https://doi.org/10.1016/j.rser.2017.09.003>.
- [2] R. Bhandari, R.R. Shah, Hydrogen as energy carrier: techno-economic assessment of decentralized hydrogen production in Germany, Renew. Energy 177 (2021) 915–931, <https://doi.org/10.1016/j.renene.2021.05.149>.
- [3] M. Carmo, D.L. Fritz, J. Mergel, D. Stolten, A comprehensive review on PEM water electrolysis, Int. J. Hydrol. Energy 38 (2013) 4901–4934, <https://doi.org/10.1016/j.ijhydene.2013.01.151>.
- [4] K. Ayers, N. Danilovic, K. Harrison, H. Xu, PEM electrolysis, a forerunner for clean hydrogen, Electrochim. Soc. Interface 30 (2021) 67–72, <https://doi.org/10.1149/2.fl6214if>.
- [5] C.V. Pham, D. Escalera-López, K. Mayrhofer, S. Cherevko, S. Thiele, Essentials of high performance water electrolyzers – from catalyst layer materials to electrode engineering, Adv. Energy Mater. 11 (2021) 2101998, <https://doi.org/10.1002/aenm.202101998>.
- [6] C. Minke, M. Suermann, B. Bensmann, R. Hanke-Rauschenbach, Is iridium demand a potential bottleneck in the realization of large-scale PEM water electrolysis?, Int. J. Hydrogen Energy, 46 (2021) 23581–23590, <https://doi.org/10.1016/j.ijhydene.2021.04.174>.
- [7] K. Nose, T.H. Okabe, Chapter 2.10 - Platinum Group Metals Production, in: S. Seetharaman (Ed.) Treatise on Process Metallurgy, Elsevier, Boston, Ir atom utilization efficiency 2014, pp. 1071–1097, <https://doi.org/10.1016/B978-0-08-096988-6.00018-3>.
- [8] J. Kibsgaard, I. Chorkendorff, Considerations for the scaling-up of water splitting catalysts, Nat. Energy 4 (2019) 430–433, <https://doi.org/10.1038/s41560-019-0407-1>.
- [9] B.-S. Lee, S.H. Ahn, H.-Y. Park, I. Choi, S.J. Yoo, H.-J. Kim, D. Henkensmeier, J. Y. Kim, S. Park, S.W. Nam, K.-Y. Lee, J.H. Jang, Development of electrodeposited IrO₂ electrodes as anodes in polymer electrolyte membrane water electrolysis, Appl. Catal., B 179 (2015) 285–291, <https://doi.org/10.1016/j.apcatb.2015.05.027>.
- [10] S. Choe, B.-S. Lee, M.K. Cho, H.-J. Kim, D. Henkensmeier, S.J. Yoo, J.Y. Kim, S. Y. Lee, H.S. Park, J.H. Jang, Electrodeposited IrO₂/Ti electrodes as durable and cost-effective anodes in high-temperature polymer-membrane-electrolyte water electrolyzers, Appl. Catal., B 226 (2018) 289–294, <https://doi.org/10.1016/j.apcatb.2017.12.037>.
- [11] M.B. Gawande, A. Goswami, T. Asefa, H. Guo, A.V. Biradar, D.-L. Peng, R. Zboril, R.S. Varma, Core–shell nanoparticles: synthesis and applications in catalysis and electrocatalysis, Chem. Soc. Rev. 44 (2015) 7540–7590, <https://doi.org/10.1039/C5CS00343A>.
- [12] A. Lim, J. Kim, H.-J. Lee, H.-J. Kim, S.J. Yoo, J.H. Jang, H. Young Park, Y.-E. Sung, H.S. Park, Low-loading IrO₂ supported on Pt for catalysis of PEM water electrolysis and regenerative fuel cells, Appl. Catal., B 272 (2020), 118955, <https://doi.org/10.1016/j.apcatb.2020.118955>.
- [13] P. Patsalas, N. Kalfagiannis, S. Kassavetis, G. Abadias, D.V. Bellas, C. Lekka, E. Lidorikis, Conductive nitrides: growth principles, optical and electronic properties, and their perspectives in photonics and plasmonics, Mater. Sci. Eng. R. Rep. 123 (2018) 1–55, <https://doi.org/10.1016/j.mser.2017.11.001>.
- [14] X. Peng, C. Pi, X. Zhang, S. Li, K. Huo, P.K. Chu, Recent progress of transition metal nitrides for efficient electrocatalytic water splitting, Sustain. Energy Fuels 3 (2019) 366–381, <https://doi.org/10.1039/C8SE00525G>.
- [15] B.M. Tackett, W. Sheng, S. Kattel, S. Yao, B. Yan, K.A. Kuttyiel, Q. Wu, J.G. Chen, Reducing iridium loading in oxygen evolution reaction electrocatalysts using core–shell particles with nitride cores, ACS Catal. 8 (2018) 2615–2621, <https://doi.org/10.1021/acscatal.7b04410>.
- [16] H.-Y. Jeong, D.-g Kim, S.G. Akpe, V.K. Paidi, H.S. Park, S.-H. Lee, K.-S. Lee, H. C. Ham, P. Kim, S.J. Yoo, Hydrogen-mediated thin Pt layer formation on Ni3N nanoparticles for the oxygen reduction reaction, ACS Appl. Mater. Interfaces 13 (2021) 24624–24633, <https://doi.org/10.1021/acsmami.1c01544>.
- [17] K.A. Kuttyiel, K. Sasaki, Y. Choi, D. Su, P. Liu, R.R. Adzic, Nitride stabilized PtNi core–shell nanocatalyst for high oxygen reduction activity, Nano Lett. 12 (2012) 6266–6271, <https://doi.org/10.1021/nl303362s>.
- [18] K.A. Kuttyiel, Y. Choi, S.-M. Hwang, G.-G. Park, T.-H. Yang, D. Su, K. Sasaki, P. Liu, R.R. Adzic, Enhancement of the oxygen reduction on nitride stabilized pt-M (M=Fe, Co, and Ni) core–shell nanoparticle electrocatalysts, Nano Energy 13 (2015) 442–449, <https://doi.org/10.1016/j.nanoen.2015.03.007>.
- [19] K. Yamanaka, Anodically electrodeposited iridium oxide films (AEIROF) from alkaline solutions for electrochromic display devices, Jpn. J. Appl. Phys. 28 (1989) 632–637, <https://doi.org/10.1143/jjap.28.632>.
- [20] S.A.M. Marzouk, Improved electrodeposited iridium oxide pH sensor fabricated on etched titanium substrates, Anal. Chem. 75 (2003) 1258–1266, <https://doi.org/10.1021/ac0261404>.
- [21] P. Steegstra, E. Ahlberg, Involvement of nanoparticles in the electrodeposition of hydrous iridium oxide films, Electrochim. Acta 68 (2012) 206–213, <https://doi.org/10.1016/j.electacta.2012.02.058>.

[22] M. Bühler, P. Holzapfel, D. McLaughlin, S. Thiele, From catalyst coated membranes to porous transport electrode based configurations in PEM water electrolyzers, *J. Electrochem. Soc.* 166 (2019) F1070–F1078, <https://doi.org/10.1149/2.0581914jes>.

[23] J. Mo, Z. Kang, T. Retterer Scott, A. Cullen David, J. Toops Todd, B. Green Johny, M. Mench Matthew, F.-Y. Zhang, Discovery of true electrochemical reactions for ultrahigh catalyst mass activity in water splitting, *Sci. Adv.* 2 (2016), e1600690, <https://doi.org/10.1126/sciadv.1600690>.

[24] Q.-q Xiong, J.-p Tu, X.-h Xia, X.-y Zhao, C.-d Gu, X.-l Wang, A three-dimensional hierarchical Fe₂O₃@NiO core/shell nanorod array on carbon cloth: a new class of anode for high-performance lithium-ion batteries, *Nanoscale* 5 (2013) 7906–7912, <https://doi.org/10.1039/C3NR02258G>.

[25] T.-Y. Yang, H.-Y. Kang, K. Jin, S. Park, J.-H. Lee, U. Sim, H.-Y. Jeong, Y.-C. Joo, K. T. Nam, An iron oxide photoanode with hierarchical nanostructure for efficient water oxidation, *J. Mater. Chem. A* 2 (2014) 2297–2305, <https://doi.org/10.1039/C3TA13830E>.

[26] M. Widenmeyer, T.C. Hansen, E. Meissner, R. Niewa, Formation and decomposition of iron nitrides observed by in situ powder neutron diffraction and thermal analysis, *Z. Anorg. Allg. Chem.* 640 (2014) 1265–1274, <https://doi.org/10.1002/zaac.201300676>.

[27] S.E. O'Sullivan, S.-K. Sun, S.M. Lawson, M.C. Stennett, F. Chen, Y. Masubuchi, C. L. Corkhill, N.C. Hyatt, Low-temperature nitridation of Fe₃O₄ by reaction with NaNH₂, *Inorg. Chem.* 60 (2021) 2553–2562, <https://doi.org/10.1021/acs.inorgchem.0c03452>.

[28] M. Graffouté, C. Petitjean, A. Diama, J.F. Pierson, J.M. Gremec, C. Rousselot, Structural investigations of iron oxynitride multilayered films obtained by reactive gas pulsing process, *Surf. Coat. Technol.* 272 (2015) 158–164, <https://doi.org/10.1016/j.surfcoat.2015.04.010>.

[29] E.A. Bel'skaya, E.Y. Kulyamina, Electrical resistivity of titanium in the temperature range from 290 to 1800 K, *High. Temp.* 45 (2007) 785–796, <https://doi.org/10.1134/S0018151X07060090>.

[30] E. Yoo, J.H. Moon, Y.S. Jeon, Y. Kim, J.-P. Ahn, Y.K. Kim, Electrical resistivity and microstructural evolution of electrodeposited Co and Co-W nanowires, *Mater. Charact.* 166 (2020), 110451, <https://doi.org/10.1016/j.matchar.2020.110451>.

[31] T. Yamashita, P. Hayes, Analysis of XPS spectra of Fe²⁺ and Fe³⁺ ions in oxide materials, *Appl. Surf. Sci.* 254 (2008) 2441–2449, <https://doi.org/10.1016/j.apsusc.2007.09.063>.

[32] A.P. Grosvenor, B.A. Kobe, M.C. Biesinger, N.S. McIntyre, Investigation of multiplet splitting of Fe 2p XPS spectra and bonding in iron compounds, *Surf. Interface Anal.* 36 (2004) 1564–1574, <https://doi.org/10.1002/sia.1984>.

[33] G. Greczynski, L. Hultman, Towards reliable X-ray photoelectron spectroscopy: sputter-damage effects in transition metal borides, carbides, nitrides, and oxides, *Appl. Surf. Sci.* 542 (2021), 148599, <https://doi.org/10.1016/j.apsusc.2020.148599>.

[34] I.S. Zhidkov, A.I. Kukharenko, A.V. Makarov, R.A. Savrai, N.V. Gavrilov, S. O. Cholakh, E.Z. Kurmaev, XPS characterization of surface layers of stainless steel nitrided in electron beam plasma at low temperature, *Surf. Coat. Technol.* 386 (2020), 125492, <https://doi.org/10.1016/j.surfcoat.2020.125492>.

[35] V. Pfeifer, T.E. Jones, J.J. Velasco Vélez, C. Massué, R. Arrigo, D. Teschner, F. Girsdsies, M. Scherzer, M.T. Greiner, J. Allan, M. Hashagen, G. Weinberg,

S. Piccinin, M. Hävecker, A. Knop-Gericke, R. Schlögl, The electronic structure of iridium and its oxides, *Surf. Interface Anal.* 48 (2016) 261–273, <https://doi.org/10.1002/sia.5895>.

[36] M.D. Obradović, B.D. Balanč, U.Č. Laćnjevac, S.L. Gojković, Electrochemically deposited iridium-oxide: estimation of intrinsic activity and stability in oxygen evolution in acid solution, *J. Electroanal. Chem.* 881 (2021), 114944, <https://doi.org/10.1016/j.jelechem.2020.114944>.

[37] L. Il'yukhina, S. Sunde, R.G. Haeverkamp, Electronic structure and growth of electrochemically formed iridium oxide films, *J. Electrochem. Soc.* 164 (2017) F1662–F1670, <https://doi.org/10.1149/2.1351714jes>.

[38] C. Liu, K. Wippermann, M. Rasinski, Y. Suo, M. Shviro, M. Carmo, W. Lehnert, Constructing a multifunctional interface between membrane and porous transport layer for water electrolyzers, *ACS Appl. Mater. Interfaces* 13 (2021) 16182–16196, <https://doi.org/10.1021/acsami.0c20690>.

[39] P. Lettenmeier, R. Wang, R. Abouatallah, S. Helmly, T. Morawietz, R. Hiesgen, S. Kolb, F. Burggraf, J. Kallo, A.S. Gago, K.A. Friedrich, Durable membrane electrode assemblies for proton exchange membrane electrolyzer systems operating at high current densities, *Electrochim. Acta* 210 (2016) 502–511, <https://doi.org/10.1016/j.electacta.2016.04.164>.

[40] P. Lettenmeier, S. Kolb, N. Sata, A. Fallisch, L. Zielke, S. Thiele, A.S. Gago, K. A. Friedrich, Comprehensive investigation of novel pore-graded gas diffusion layers for high-performance and cost-effective proton exchange membrane electrolyzers, *Energ. Environ. Sci.* 10 (2017) 2521–2533, <https://doi.org/10.1039/C7EE01240C>.

[41] M. Yagi, E. Tomita, T. Kuwabara, Remarkably high activity of electrodeposited IrO₂ film for electrocatalytic water oxidation, *J. Electroanal. Chem.* 579 (2005) 83–88, <https://doi.org/10.1016/j.jelechem.2005.01.030>.

[42] S.M. Alia, S. Stariha, R.L. Borup, Electrolyzer durability at low catalyst loading and with dynamic operation, *J. Electrochem. Soc.* 166 (2019) F1164–F1172, <https://doi.org/10.1149/2.0231915jes>.

[43] A.C. Fernandes, E.A. Ticianelli, A performance and degradation study of Nafion 212 membrane for proton exchange membrane fuel cells, *J. Power Sources* 193 (2009) 547–554, <https://doi.org/10.1016/j.jpowsour.2009.04.038>.

[44] Z. Kang, M. Pak, G. Bender, Introducing a novel technique for measuring hydrogen crossover in membrane-based electrochemical cells, *Int. J. Hydrog. Energy* 46 (2021) 15161–15167, <https://doi.org/10.1016/j.ijhydene.2021.02.054>.

[45] T. Schuler, T.J. Schmidt, F.N. Büchi, Polymer electrolyte water electrolysis: correlating performance and porous transport layer structure: part II. Electrochemical performance analysis, *J. Electrochem. Soc.* 166 (2019) F555–F565, <https://doi.org/10.1149/2.1241908jes>.

[46] M. Mandal, M. Moore, M. Secanell, Measurement of the protonic and electronic conductivities of PEM water electrolyzer electrodes, *ACS Appl. Mater. Interfaces* 12 (2020) 49549–49562, <https://doi.org/10.1021/acsami.0c12111>.

[47] A. Vishnyakov, A.V. Neimark, Molecular dynamics simulation of microstructure and molecular mobilities in swollen nafion membranes, *J. Phys. Chem. B* 105 (2001) 9586–9594, <https://doi.org/10.1021/jp0102567>.

[48] A. Vishnyakov, A.V. Neimark, Self-assembly in nafion membranes upon hydration: water mobility and adsorption isotherms, *J. Phys. Chem. B* 118 (2014) 11353–11364, <https://doi.org/10.1021/jp04975u>.